

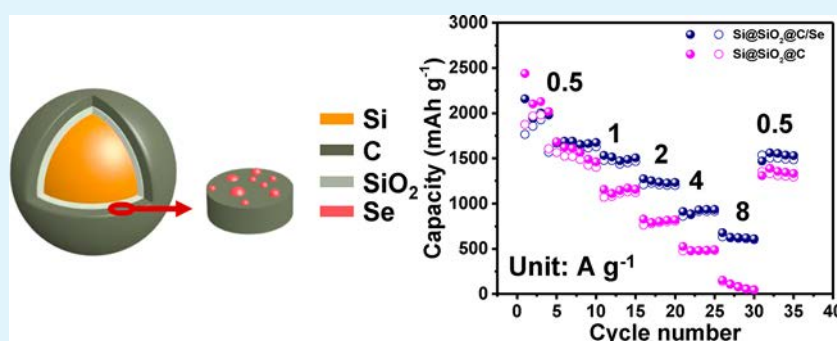
Improving Cycling Performance of Si-Based Lithium Ion Batteries Anode with Se-Loaded Carbon Coating

Xin Gu,^{§,†} Wang Tian,^{§,†} Xiaoqiang Tian,[†] Yaqin Ding,[†] Xiaofeng Jia,[†] Li Wang,[‡] and Yong Qin^{*,†,‡}

[†]Institute of Nanoscience and Nanotechnology, School of Physical Science and Technology, Lanzhou University, Gansu 730000, China

[‡]Institute of Applied Magnetism, Key Laboratory for Magnetism and Magnetic Material of the Education Ministry, Department of Physics, Lanzhou University, Gansu 730000, China

Supporting Information



ABSTRACT: Poor cycling stability and rate capability significantly limit the commercial applications of silicon (Si) anode, due to the huge volume change and poor electronic and ionic conductivity of Si. Combining Si with SiO₂ and carbon (C) can effectively improve the structural stability of electrode, but common carbon coating still suffers from the problem of comparatively low ionic conductivity. Here we designed and developed a core–shell structural Si@SiO₂@C/Se anode with high ionic conductivity and structural stability by loading selenium (Se) into a carbon framework. Remarkably, it exhibits a high rate capability (612 mAh g⁻¹ at 8 A g⁻¹) and ultrahigh initial coulombic efficiency (80.8%), which is much higher than ordinary Si/SiO₂-based anode (50–60%). In addition, it shows an excellent cycling performance, which is about 1560 mAh g⁻¹ after 150 charging/discharging cycles at the current density of 0.5 A g⁻¹. This work provides a new technology to design high capacity alloy-type lithium-ion batteries (LIBs) anode.

KEYWORDS: silicon, lithium ion batteries anode, carbon/selenium composite, rate capability, ionic conductivity

INTRODUCTION

LIBs are of great importance in our daily life as they are indispensably used for intelligent devices, battery electric vehicles and other energy storage systems.^{1–3} Therefore, many high-energy density materials have been studied for LIBs to meet the requirement for high specific capacity and cyclability.⁴ Among the potential LIBs anode materials, Si is a promising candidate for high-performance LIB anodes due to following reasons: first, Si has an ultrahigh theoretical specific capacity (~3579 mAh g⁻¹, Li₁₅Si₄),⁵ which is much higher than that of commercial graphite (~372 mAh g⁻¹).⁶ Additionally, Si has a moderate lithiation voltage plateau (<0.5 V vs Li⁺/Li), which can give a good balance between a reasonable open circuit potential retention and avoidance of the dendrite formation resulting from the lithium plating.⁷ Moreover, Si is the second most abundant element in the Earth's crust and is environmentally friendly.⁸ Unfortunately, it is still quite challenging to fulfill the application of a Si anode in commercial LIBs, whose huge volume change (~300%) during lithium ion insertion/extraction processes would cause severe

capacity fading, resulting from the cracking and pulverization together with the disconnection to the current collector of Si anode.^{9,10} Furthermore, due to the relatively low electrode potential of lithium ion insertion/extraction (below to ~1 V vs Li⁺/Li), it is thermodynamically favorable for the carbonate electrolyte decomposition. The decomposed products would deposit and form a solid-electrolyte interphase (SEI). The SEI stability at the interface between electrode and the electrolyte is critical for obtaining long cycling life.¹¹ Different from the commercial graphite that forms dense and stable SEI and prevents further side chemical reactions, a huge volume change during charge/discharge cycles in Si anode results in the instability of SEI. The continual crush and re-formation of SEI consume lithium ions and lead to the fast decay of capacity.^{12,13} Therefore, a stable structure and excellent mechanical properties of Si-based anode are necessary.

Received: April 25, 2019

Accepted: June 14, 2019

Published: June 14, 2019

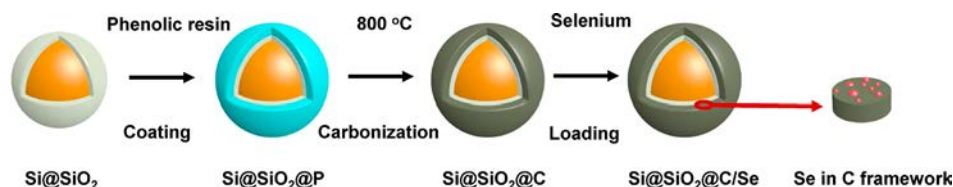


Figure 1. Synthesis process of Si@SiO₂@C/Se NPs.

The volume expansion can be effectively alleviated by reducing the size of bulk Si into nanoscale to improve the cycling performance. Recently, various nanostructural Si anodes have been designed, such as nanowires (NWs), nanotubes (NTs), nanofilm, nanoparticles (NPs), and so on.^{14–16} Most of these nanostructures are fabricated by a series of complex and costly methods like chemical vapor deposition (CVD) and magnetron sputtering.^{17,18} Furthermore, these nanostructural Si materials are still directly exposed to the electrolyte, so it is hard to form a thin and stable SEI film. To resolve this problem, conformal coatings are extensively researched to avoid the immediate contact between Si and electrolyte. Some coating materials have been fabricated with a good chemical stability during Si redox process, such as a part of metal oxides, conductive polymers and carbon.^{19–21} Recently, the Si/SiO_x/C composite anodes were investigated widely, because SiO_x in this matrix can effectively alleviate the volume change of Si and C provides a conductive framework and structural support.²² But the irreversible reaction during first cycle, poor electric and ionic conductivity of SiO_x result to poor rate capability and low initial coulombic efficiency (ICE) (50–60%), which seriously restricts its commercial application.²³ Besides, charge–discharge reaction rate is diffusion controlled.²⁴ Therefore, another key character of high-performance anode is having high ionic conductivity to reduce the resistance of the diffusion of lithium ion. Relatively high ionic conductivity means that it can diminish the polarization effect caused by the difference of conduction efficiency between lithium ion and electron.

Se has a similar lithium ion insertion/extraction behavior with sulfur and possesses a much higher ionic conductivity. Meanwhile, Se exhibits a relative high-voltage plateau (1.5–3 V vs Li⁺/Li), and lithiated Se can improve the lithium ion transmission efficiency.^{25,26} However, due to the dissolveability of polyselenide intermediates, bulk Se exhibits an unstable cycling performance. But the C/Se composite Se composed with microporous carbon can give an interaction between Se and the carbon framework to restrain the shuttle effect of polyselenide.^{27,28} Therefore, the C/Se composite can be used as a promising coating candidate material for Si-based anode to get longer cycling life and higher rate capability.

Herein, we design a high-performance Si-based anode material consisting of a core of Si with a surface oxide layer and a shell of C/Se composites (Si@SiO₂@C/Se). The innovative C/Se composite coating layer with high ionic conductivity and mechanical properties has been synthesized and applied as the coating layer of the Si-based anode. The Si@SiO₂@C/Se anode maintains a high specific capacity of 1560 mAh g⁻¹ after 150 charge/discharge cycles at the current density of 0.5 A g⁻¹ and a favorable rate capability of 612 mAh g⁻¹ at 8 A g⁻¹. Furthermore, a series of electrochemical and morphological characterization show that the ionic conductivity and structural stability of electrode have been improved by introducing a C/Se composite coating layer into Si-based

anode. A new method for designing high-performance Si-based LIBs anode is provided.

RESULTS AND DISCUSSION

Figure 1 illustrates the synthesis process of Si@SiO₂@C/Se NPs. The Si@SiO₂ NPs are commercially available Si NPs with ~2 nm thick native oxide layer and the average grain size is about 50 nm. (Figure S1). During the first discharge process, the SiO₂ outlayer can react with Li to form a Si, Li_xO, and lithium silicate passivation layer, which can provide a supporting function to restrain the volume change of Si in subsequent cycles to improving the cycling performance of electrode.²⁹ The resorcinol/formaldehyde (RF) resin polymer shell is used as carbon precursor, which is synthesized by a sol–gel process.³⁰ Then, the microporous Si@SiO₂@C NPs are obtained by carbonization under an argon atmosphere. Lastly, the loading of Se is realized through a melting–diffusion process. The Si@SiO₂@C/Se NPs present a core–shell structure consisting of a core of Si@SiO₂ and a ~8 nm thick shell of the C/Se composite (Figure S2), which can be further revealed by the high-resolution transmission electron microscopy (HRTEM) image (Figure 2a). Meanwhile, it

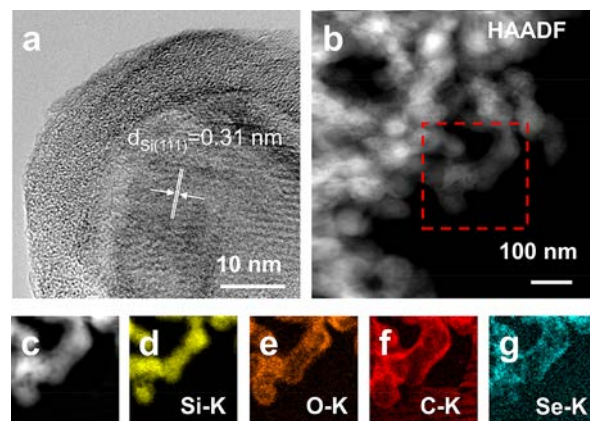


Figure 2. (a) HRTEM image of Si@SiO₂@C/Se. (b, c) HAADF-STEM images of Si@SiO₂@C/Se and its corresponding elemental maps of (d) Si, (e) O, (f) C, and (g) Se.

shows an interplanar spacing of 0.31 nm, which corresponds to Si (111) planes (JCPDS No. 27-1402). The distribution of Si, O, C, and Se are characterized by high-angle annular dark field (HAADF) scanning transmission electron microscopy (STEM). As shown in Figure 2b–g, the distribution of Si, C, and O demonstrates that the SiO₂ layer is distributed on the surface of Si and C is coated on the SiO₂ layer. In addition, the Se map matches well with the C map, indicating Se is confined in the host of the microporous carbon coating layer uniformly. The XRD patterns of samples are shown in Figure 3a, the sharp diffraction peaks in Si@SiO₂@C and Si@SiO₂C/Se patterns all match well with the Si standard card (JCPDS No.

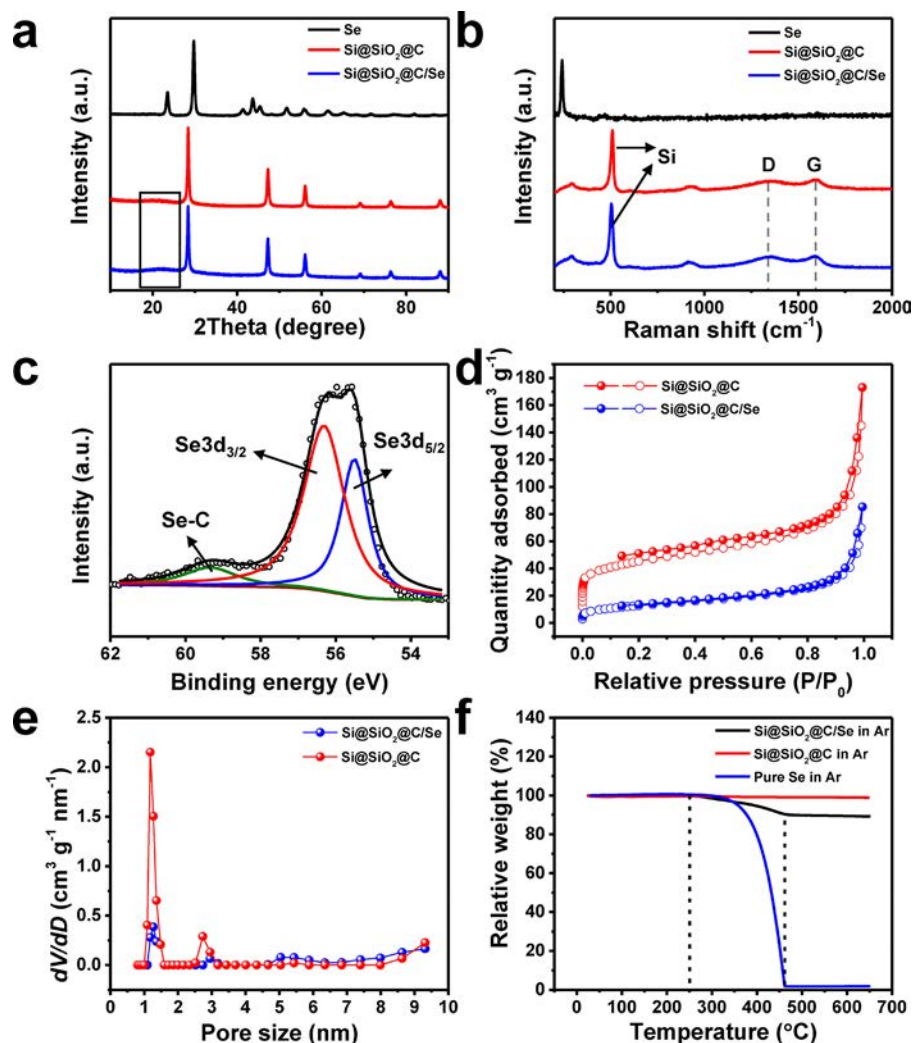


Figure 3. (a) XRD pattern and (b) Raman spectra of Se, Si@SiO₂@C, and Si@SiO₂@C/Se. (c) XPS spectra of Se 3d. (d) N₂ adsorption/desorption isotherms and (e) pore size distributions of Si@SiO₂@C and Si@SiO₂@C/Se. (f) TGA curves of Si@SiO₂@C, Si@SiO₂@C/Se, and pure Se. The boxed part in the XRD pattern shown in (a) may come from diffraction of carbon or SiO₂.

27–1402), A weak broad peak appears around 23°, which comes from to the diffraction of SiO₂ or amorphous carbon.³¹ Therefore, no peak of Se is observed in Si@SiO₂@C and Si@SiO₂@C/Se, demonstrating that Se exists in a highly dispersed amorphous state. Raman spectra of Se, Si@SiO₂@C, and Si@SiO₂@C/Se are displayed in Figure 3b, and no obvious peaks of Se appear in the spectra of Si@SiO₂@C/Se, which agrees with the XRD pattern, indicating that amorphous Se occupies the pores of carbon.³² The X-ray photoelectron spectroscopy (XPS) is carried out to further examine chemical states of the Se in the carbon framework (Figure 3c). The fitted peaks at 56.3 and 55.5 eV are assigned to Se 3d 3/2 and Se 3d 5/2, respectively, due to the spin–orbit coupling. In addition, there is a weak broad peak at 59.3 eV, which attributed to the Se–C bonds formed by the reaction between Se and carbonyl groups during the melting–diffusion process.³³

In order to further confirm the occupation of Se in the carbon framework, the nitrogen adsorption/desorption isotherms of Si@SiO₂@C and Si@SiO₂@C/Se are shown in Figure 3d, which displays a typical type I curve and reflects a microporous-rich structure of Si@SiO₂@C. Figure 3e describes pore size distribution of the two samples. With the loading of Se into the microporous carbon framework, the

BET surface area and adsorption pore volume dramatically decrease from 149.03 m² g⁻¹ and 0.27 cm³ g⁻¹ to 44.99 m² g⁻¹ and 0.13 cm³ g⁻¹ respectively, indicating that micropores in Si@SiO₂@C are occupied by Se. In order to calculate the mass fraction of Se in Si@SiO₂@C/Se, thermogravimetric analysis (TGA) curves of pure Se, Si@SiO₂@C, and Si@SiO₂@C/Se are tested under an argon atmosphere in Figure 3f, respectively. The Se will evaporate completely between 250 and 460 °C under an argon atmosphere, and its content in Si@SiO₂@C/Se is 10.02 wt %. Otherwise, as shown in Figure S3, the C content in Si@SiO₂@C is 17.5 wt %.

The electrochemical performances of both Si@SiO₂@C and Si@SiO₂@C/Se are measured using conventional carbonate based electrolyte. The specific capacity of two electrodes is calculated on the basis of the mass of active materials. The CV curves of two electrodes are shown in Figure 4a,b, respectively. The CV curves are tested under the scan rate of 0.1 mV s⁻¹ in the voltage window 0.01–3 V. In the voltage window 0.01–1.2 V, both electrodes demonstrate the typical CV curves of Si. The appearance of a unique reduction peak around 0.3 V in the first cycle and disappearance in subsequent cycles can be attributed to the irreversible reduction reaction of SiO₂ with Li to form Si, Li_xO, and a series of lithium silicate.³⁴

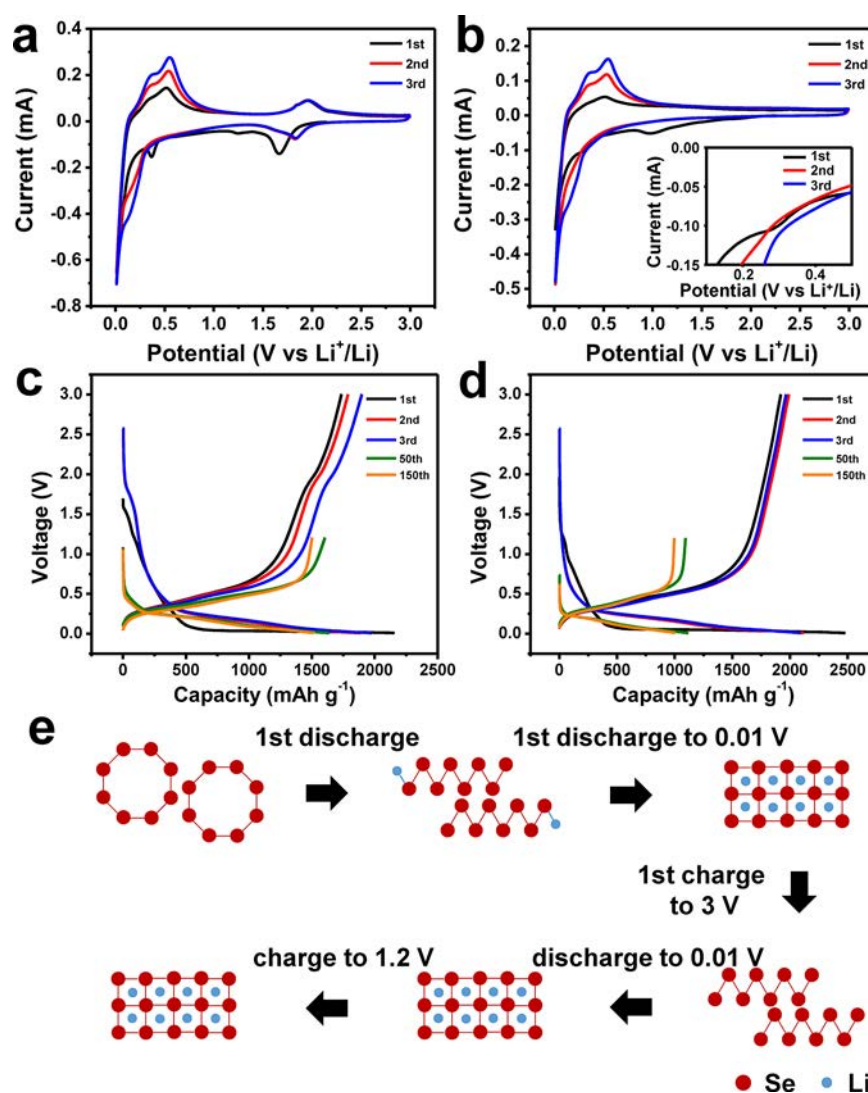


Figure 4. CV curves for (a) Si@SiO₂@C/Se and (b) Si@SiO₂@C electrodes. Charging/discharging curves of the (c) Si@SiO₂@C/Se and (d) Si@SiO₂@C electrodes. (e) Proposed delithiation/lithiation processes of Se in C framework.

The sharp reduction peak below 0.1 V is correlated with the lithiation process of Si. In the cathodic scan curves, the two oxidation peaks at 0.37 and 0.55 V are attributed to the delithiation process of Li_xSi.³⁵ Noticeably, there is one pair of redox peaks in the CV curves of Si@SiO₂@C/Se in the voltage window 1.2–3 V, which can be attributed to the redox process of Se with Li. In addition, only one pair of redox peaks indicates the good reversibility and stability of Li₂Se and Se with no soluble polyselenide forming during cycling.³² The appearance of a reduction peak at 1.6 V in the first cycle and following transfer to 1.8 V in subsequent cycles can be attributed to the activation process of Se in the first cycle.³⁶ In contrast, no obvious peak appears in the CV curves of Si@SiO₂@C in the voltage window 1.2–3.0 V. A similar phenomenon can be observed in the galvanostatic charge/discharge voltage profiles of two electrodes in the first three cycles shown in Figure 4c,d. When the voltage window changes to 0.01–1.2 V after the third cycle, there is only one pair of obvious voltage plateaus, which account for the only lithiation/delithiation process of Si in this voltage window. The reaction mechanism of Se in the C framework is proposed and shown in Figure 4e. First, the ring-like Se_n transfers to chain-like Se_n, and

then the lithium ion inserts chain-like Se_n to form Li₂Se after the first discharging process until 0.01 V. When charged to 3 V, chain-like Se_n re-forms instead of forming the original ring-like Se_n.³⁷ When discharged to 0.01 V, Li₂Se forms again, but when charged to 1.2 V, Li₂Se still exists in the C framework, which is in accordance with the CV and galvanostatic discharge/charge voltage profiles in the fourth cycle (Figure S4). There is no obvious oxidation peak and voltage plateau in the fourth cycle, indicating that Li₂Se in the carbon framework is stable during cycling.

The redox reaction rate depends on diffusion of lithium ions. The diffusion coefficient (D_{Li^+}) can be calculated on the basis of the Randles–Sevcik eq (eq 1) for a semi-infinite diffusion of lithium ion.

$$i_p = 0.4663nF\sqrt{\frac{nFD}{RT}}AC\sqrt{\nu} \quad (1)$$

where the R , T , and F are the gas constant, temperature, and Faraday constant, respectively. A , C , and n are the electrode area, concentration of lithium ion, and charge of transfer electrons, respectively. D , i_p , and ν stand for the lithium ion diffusion coefficient, peak current, and voltage scan rate,

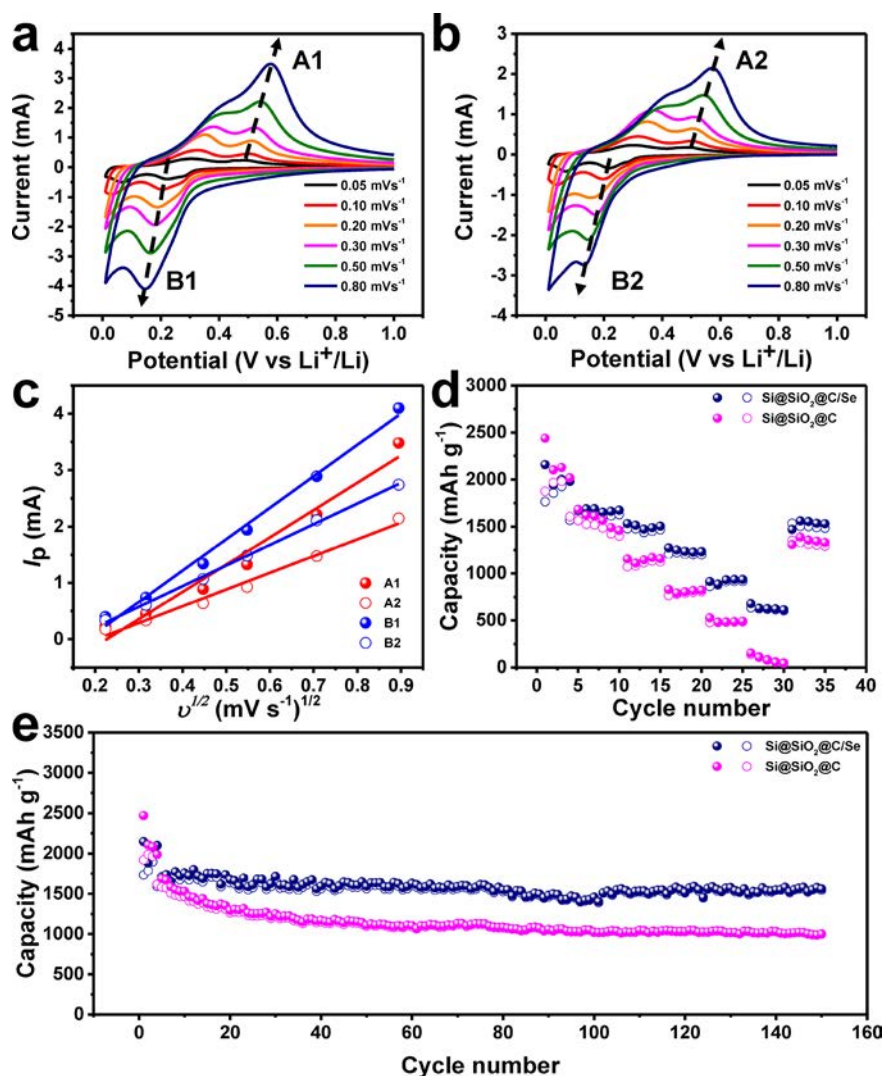


Figure 5. CV curves of (a) Si@SiO₂@C/Se and (b) Si@SiO₂@C electrodes at different scan rates. (c) Linear relationship of peak currents vs $V^{1/2}$ $s^{-1/2}$ and the corresponding linear fits. Comparison of (d) rate capability at different current densities and (e) cycle performance at 0.5 A g^{-1} for the Si@SiO₂@C and Si@SiO₂@C/Se electrodes.

respectively. Both electrodes are prepared and tested by the same procedure. Therefore, the Randles–Sevcik equation can be simplified as

$$i_p = a\sqrt{D}\sqrt{v} \quad (2)$$

The a in eq 2 can be considered as a constant and $a\sqrt{D}$ is defined as apparent diffusion coefficient of lithium ion in the cells.³⁸ The CV curves of two electrodes after 20 cycles in the voltage window of 0.01–1.2 V at the scan rate from 0.05 to 0.8 mV s^{-1} are shown in Figure 5a,b, and the values of current peak in CV curves depend on the lithium ion diffusion and scan rate. The linear fitting curves are displayed in Figure 5c, indicating that the lithium ion diffusion coefficient of Si@SiO₂@C/Se is obviously higher than that of Si@SiO₂@C. It also illustrates indicates that loading of Se into the carbon framework significantly shortens the lithium ion transport pathway and accelerates the diffusion rate of the lithium ion, both of which lead to the improvement of reaction kinetics, lithium storage, and rate capability of the Si@SiO₂@C/Se electrode. In order to confirm this deduction, Figure 5d displays the comparison of the rate capability of two

electrodes, where the voltage window is set at 0.01–3 V in first three cycles to ensure the complete reaction of Se, and the voltage window is changed to 0.01–1.2 V in the subsequent cycles. The specific capacities of 1505, 1232, 936, and 612 mAh g^{-1} are achieved at current densities of 1, 2, 4, and 8 A g^{-1} , respectively. In order to further realize the stability of the Si@SiO₂@C/Se electrode during the high-rate charge/discharge process, the current density is returned back to 0.5 A g^{-1} , and the specific capacity recovers to 1559 mAh g^{-1} , which demonstrates its good structural stability. Remarkably, at the high rate of 8 A g^{-1} , the specific capacity of the Si@SiO₂@C/Se electrode is 13.9 times higher than that of the Si@SiO₂@C electrode (44 mAh g^{-1}). In the meantime, the Si@SiO₂@C/Se electrode exhibits an excellent cycling performance. The comparison of cycling performance between the two electrodes is shown in Figure 5e. The Si@SiO₂@C/Se electrode exhibits an excellent cycling stability, a high reversible capacity that can be maintained at 1560 mAh g^{-1} after 150 cycles, and about 91.2% capacity retention (vs fifth cycle), which is about 0.06% capacity fading per cycle. The excellent cycling stability is attributed to the superior structure stability of the C/Se composite coating layer. Noticeably, the specific capacity of the

Si@SiO₂@C/Se electrode achieves 2149 mAh g⁻¹ during the first discharge, which is lower than that of the Si@SiO₂@C anode because of the existence of low theoretical specific capacity Se in the Si@SiO₂@C/Se electrode. And the specific capacity of the Si@SiO₂@C/Se electrode is reduced when the voltage window is transferred from 0.01–3 to 0.01–1.2 V, which can be attributed to Se no longer participating in the redox reaction during cycling. In contrast, the Si@SiO₂@C electrode has a severe decay in the first 20 cycles, which is about 59.2% capacity retention (vs fifth cycle). Otherwise, the Si@SiO₂@C/Se electrode exhibits a high ICE (80.8%), which is a large progress for Si/SiO₂-based anode materials. And the Coulombic efficiency (CE) of Si@SiO₂@C/Se is higher than that of Si@SiO₂@C in subsequent cycles and maintains a value over 98% in the 150th cycle. (Figure S5). A higher CE means less irreversible reaction in charge/discharge cycles due to the fewer structure changes and more stable SEI formed on the surface of electrode during cycling.

Compared with reported Si/SiO_x/C anode materials, Si@SiO₂@C/Se has shown a competitive energy storage capability (Table 1). The specific capacity of this innovative anode at

Table 1. Electrochemical Performance of the Si@SiO₂@C/Se Electrode Compared with Si-Based Anode Materials in Previous Works

materials	cycling stability (mAh g ⁻¹)/cycles/current density (A g ⁻¹)	rate capability (mAh g ⁻¹)/current density (A g ⁻¹)	ICE (%)	ref
double core-shell structured Si@SiO ₂ @C/Se nanocomposite	1560/150/0.5	612/8	80.8	this work
Si@SiO ₂ /C composite	1070/200/0.42	586/8.4	61	34
annealed Si/SiO _x /PAN composite	988/100/0.1	800/1	58.4	39
amorphous-Si@SiO _x /C composite	1230/100/0.5		77	40
boron doping Si/SiO ₂ /C	1279/100/0.5	685/6.4	71	22
amorphous Si@SiO _x /Cr/C	810/200/0.1	570/0.8	61	41
carbon coated Si/SiO _x nanospheres	740/100/0.2	825/2	78	42
Si@SiO _x /Ni/graphite composite	742.3/100/0.1		60.1	43
Si-SiO _x -cristobalite/graphite	990/150/0.1/	380/1.6	63.2	44
porous Si and SiO ₂ /CNTs	1200/200/0.5	800/2	70	45

different rates is higher than most reported results.^{22,34,39–45} Meanwhile, the cycling performance of Si@SiO₂@C/Se has reached a relatively high level in Si/SiO_x/C (0 < x ≤ 2) anode materials. Additionally, the ICE of Si@SiO₂@C/Se as high as 80.8% can effectively reduce the loading of the cathode material in the full cell, which makes the composites more likely commercially used.⁴⁶

Polymer-derived carbon contains a lot of defects,⁴⁷ which leads to a microporous structure of the carbon framework. In order to investigate the mechanism of enhanced structural stability by loading Se into the carbon framework, the binding energy of Se and the carbon framework is calculated by the first-principles method (details in the Supporting Information). Se can occupy the micropores in carbon, and Li is embedded

around Se. The strong bond energy between C and Se can significantly enhance the structural stability of carbon framework. According to the optical and SEM images (Figure S7 and S8), the Si@SiO₂@C/Se electrode exhibits higher structural stability than the Si@SiO₂@C electrode. After 10 cycles, plenty of active materials detached from the Cu current collector in the Si@SiO₂@C electrode. Such huge structural changes of the electrode during cycling leads to a low CE and an unstable SEI. In contrast, due to the excellent mechanical stability of the C/Se composite, the structural integrity of the Si@SiO₂@C/Se electrode is maintained during cycling. As the previous study shows, the SEI components of a Si/C-based electrode in carbonate electrolyte include Li₂CO₃, LiF, and Li₂O,⁴⁸ from which the existence and distribution of the SEI can be identified by the elements O and F to some extent. As shown in Figure 6, the surface morphology of Si@SiO₂@C/Se and Si@SiO₂@C electrodes are characterized by SEM and energy dispersive X-ray (EDX) mapping. Uniform distributions of the O and F elements on the surface of the Si@SiO₂@C/Se electrode are observed, which indicate the formation of stable SEI on the surface of the electrode, attributed to the high structural stability of the C/Se composite. In contrast, the surface morphology of the Si@SiO₂@C electrode is rougher than that of the Si@SiO₂@C/Se electrode. Meanwhile, the distributions of O and F elements are not even. These are ascribed to the huge structural changes during cycling, which result in a compromised mechanical stability of the whole electrode and an unstable SEI on the surface of the Si@SiO₂@C electrode. Consequently, the introducing of C/Se coating layer can significantly enhance the mechanical stability of Si@SiO₂@C/Se, which leads to a more stable SEI at the surface of the electrode, and a higher CE in charge/discharge cycles is obtained.

As mentioned above, the superior properties of the Si@SiO₂@C/Se anode are mainly attributed to the excellent ionic conductivity and structural stability of the C/Se composite coating layer. The migration energy of the lithium ion in Li₂Se is relatively low, even lower than that in some components of SEI (Li₂O, LiF).⁴⁹ The Li₂Se in C framework can act as a fast ion diffusion channel between Si and electrolytes, which reduces the polarization effect caused by the difference of conduction efficiency between lithium and the electron and results in high rate capability and cycle stability. In addition, Li₂Se has a stronger interaction with the carbon framework,³² which can enhance the structural stability of the C/Se composite and ensure the mechanical stability of the electrode. In the meantime, the excellent mechanical stability of the electrode can reduce adverse effects caused by the large volume change of Si particles, the pulverization and shedding of active materials, and the low CE for instance.

CONCLUSIONS

In conclusion, we have designed and synthesized a double-layer core-shell nanostructural Si-based anode with high cycling performance and ionic conductivity using an innovative C/Se composite coating layer. The Si@SiO₂@C/Se electrode exhibits a comparatively high specific capacity of 1560 mAh g⁻¹ at 0.5 A g⁻¹ after 150 charge/discharge cycles; even at high rate of 8 A g⁻¹, the specific capacity can be maintained about 612 mAh g⁻¹. Besides, this innovative LIBs anode exhibits an ultrahigh ICE of 80.8%, which is higher than those of general Si/SiO_x/C composite anodes reported before. The excellent performance can be attributed to high ionic conductivity and

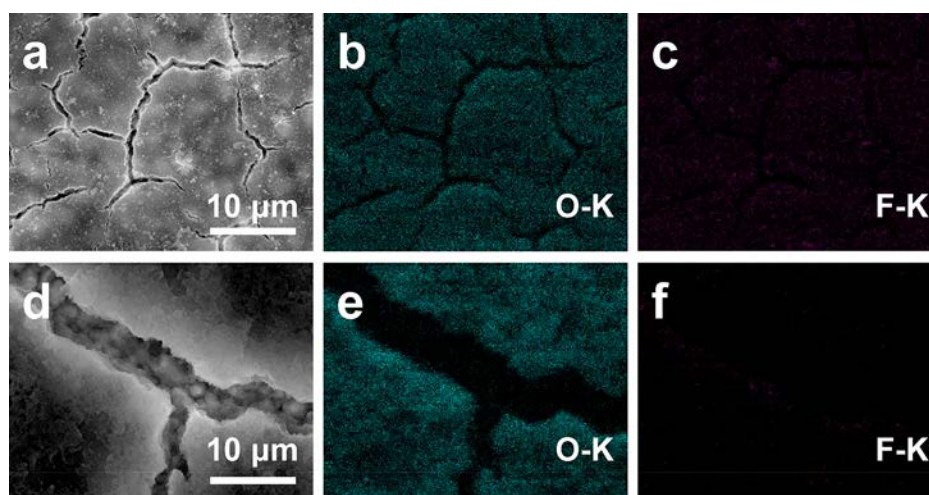


Figure 6. SEM images. O and F element distributions of (a)–(c) Si@SiO₂@C/Se and (d)–(f) Si@SiO₂@C electrodes after 10 cycles.

excellent mechanical stability of the C/Se composite coating layer compared with ordinary carbon coating. Furthermore, this core–shell Si-based nanoparticle has lower manufacturing costs and easier fabrication techniques. In addition, this innovative material as coating layer can be applied to improve the cycling performance of other high capacity alloy-type anode materials.

METHODS

Synthesis of the Core–Shell Structure Si@SiO₂@C Nanoparticles. Si nanoparticles without hydrofluoric acid treatment are with ~2 nm thickness surface native SiO₂ layer, which is named Si@SiO₂. For the synthesis of Si@SiO₂@C, 400 mg of Si@SiO₂ is dispersed in 124 mL of deionized water and the mixture is sonicated for 60 min first; then 15 mg of cetyltrimethylammonium bromide (CTAB) and 400 μL of NH₃·H₂O (28 wt %) are added in turn to the mixture, which is kept stirring for 30 min. Then 160 mg of resorcinol and 250 μL of formaldehyde are added into the mixture individually under slight stirring, and the mixture is continuously stirred for 12 h at room temperature. Si@SiO₂@P (phenolic resin) is obtained by consequently centrifuging at 9000 rpm and then washing three times using ethanol. In order to obtain the carbonizing phenolic resin coating, the dried Si@SiO₂@P powders are transferred to a tube furnace and heated under 50 sccm Ar at 800 °C for 3 h, and the heating rate is set as 5 °C min⁻¹. Finally, the core–shell structural Si@SiO₂@C nanoparticles are acquired.

Loading Se. Se is loaded into the carbon coating layer by the melting–diffusion method, which is similar to the case of the sulfur–carbon system. Si@SiO₂@C and Se powders (at the fixed Si@SiO₂@C:Se weight ratio of 2:1) are separately loaded in two quartz boats, which are then placed in a quartz tube and heated at 350 °C for 12 h in a tube furnace with flowing Ar (50 sccm) to obtain the Si@SiO₂@C/Se nanoparticles.

Characterizations. The morphology and elements distribution of the core–shell structural Si@SiO₂@C/Se NPs are investigated by TEM and HRTEM (Tecnai G2 F30, FEI, USA) equipped with an EDX analyzer (EDAX, AMTEK Co., Ltd., USA). The component of as prepared samples is characterized by XRD (Philip X'Pert pro diffractometer), Raman spectra (LabRam HR-800), and XPS (ESCALAB 250Xi electron spectrometer). N₂ sorption isotherms are measured at 77 K with an ASAP 2020 (Micromeritics, US), and the pore size distribution is calculated by the density functional theory (DFT) method from the adsorption branches of the isotherms. The Se content of Si@SiO₂@C/Se is determined by TGA (Pyris Diamond TG/DTA). The surface morphology and EDX mapping of electrode are observed by Hitachi S-4800 and FEI Apreo S.

Electrode Fabrication and Electrochemical Characterization. The slurry is prepared by mixing Si@SiO₂@C/Se, super P, and SA (weight ratio of 8:1:1); then the slurry is coated on a copper current collector and dried at 80 °C overnight. The Si@SiO₂@C/Se electrodes are sealed in 2032 coin cells to evaluate the electrochemical properties, which are assembled in an Ar-filled glovebox. Si@SiO₂@C/Se is the working electrode, Li metal foil is the counter electrode, and the Celgard 2325 membrane is used as separator; 1 M LiPF₆ is solved in ethylene carbonate and dimethyl carbonate (volume ratio of 1:1) as the electrolyte. Cells with Si@SiO₂@C are fabricated using the same procedure. The CV is measured using a CHI660E electrochemical workstation (Chen Hua Shanghai Corp., China) at the scan rate of 0.05–0.8 mV s⁻¹ in the voltage range 0.01–1.2 or 0.01–3 V. The galvanostatic charge/discharge tests are measured using a LAND CT2001A battery-testing instrument (LAND Wuhan Corp., China) at 0.01–1.2 or 0.01–3 V.

ASSOCIATED CONTENT

Supporting Information

The Supporting Information is available free of charge on the ACS Publications website at DOI: 10.1021/acsam.9b00817.

Additional figures, including TEM images, CV and TGA curves, galvanostatic discharge/charge curves, Coulombic efficiencies, first-principles method details, carbon framework images, optical and SEM images (PDF)

AUTHOR INFORMATION

Corresponding Author

*E-mail: qinyong@lzu.edu.cn.

ORCID

Yong Qin: 0000-0002-6713-480X

Author Contributions

The manuscript was written through contributions of all authors. All authors have given approval to the final version of the manuscript.

Author Contributions

[§]These authors contributed equally to this work.

Notes

The authors declare no competing financial interest.

ACKNOWLEDGMENTS

We sincerely appreciate the support from NSFC (NO. 51472111, 81702095), the National Program for Support of

Top-notch Young Professionals, the Fundamental Research Funds for the Central Universities (No. lzujbky-2018-ot04, lzujbky-2016-k02).

REFERENCES

- (1) Su, X.; Wu, Q.; Li, J.; Xiao, X.; Lott, A.; Lu, W.; Sheldon, B. W.; Wu, J. Silicon-Based Nanomaterials for Lithium-Ion Batteries: A Review. *Adv. Energy Mater.* **2014**, *4*, 1300882.
- (2) Zuo, X.; Zhu, J.; Müller-Buschbaum, P.; Cheng, Y.-J. Silicon based lithium-ion battery anodes: A chronicle perspective review. *Nano Energy* **2017**, *31*, 113–143.
- (3) Yousaf, M.; Shi, H. T. H.; Wang, Y.; Chen, Y.; Ma, Z.; Cao, A.; Naguib, H. E.; Han, R. P. S. Novel Pliable Electrodes for Flexible Electrochemical Energy Storage Devices: Recent Progress and Challenges. *Adv. Energy Mater.* **2016**, *6*, 1600490.
- (4) Balogun, M. S.; Qiu, W.; Luo, Y.; Meng, H.; Mai, W.; Onasanya, A.; Olaniyi, T. K.; Tong, Y. A review of the development of full cell lithium-ion batteries: The impact of nanostructured anode materials. *Nano Res.* **2016**, *9*, 2823.
- (5) Liang, B.; Liu, Y.; Xu, Y. Silicon-based materials as high capacity anodes for next generation lithium ion batteries. *J. Power Sources* **2014**, *267*, 469–490.
- (6) Liu, X. R.; Deng, X.; Liu, R. R.; Yan, H. J.; Guo, Y. G.; Wang, D.; Wan, L. J. Single nanowire electrode electrochemistry of silicon anode by in situ atomic force microscopy: solid electrolyte interphase growth and mechanical properties. *ACS Appl. Mater. Interfaces* **2014**, *6*, 20317–20323.
- (7) Yao, Y.; McDowell, M. T.; Ryu, I.; Wu, H.; Liu, N.; Hu, L.; Nix, W. D.; Cui, Y. Interconnected silicon hollow nanospheres for lithium-ion battery anodes with long cycle life. *Nano Lett.* **2011**, *11*, 2949–2954.
- (8) Wu, H.; Cui, Y. Designing nanostructured Si anodes for high energy lithium ion batteries. *Nano Today* **2012**, *7*, 414–429.
- (9) Liu, X. H.; et al. Size-dependent fracture of silicon nanoparticles during lithiation. *ACS Nano* **2012**, *6*, 1522–1531.
- (10) McDowell, M. T.; Lee, S. W.; Harris, J. T.; Korgel, B. A.; Wang, C.; Nix, W. D.; Cui, Y. In situ TEM of two-phase lithiation of amorphous silicon nanospheres. *Nano Lett.* **2013**, *13*, 758–764.
- (11) Luo, W.; Wang, Y.; Wang, L.; Jiang, W.; Chou, S. L.; Dou, S. X.; Liu, H. K.; Yang, J. Silicon/Mesoporous Carbon/Crystalline TiO₂ Nanoparticles for Highly Stable Lithium Storage. *ACS Nano* **2016**, *10*, 10524–10532.
- (12) Nadimpalli, S. P. V.; Sethuraman, V. A.; Dalavi, S.; Lucht, B.; Chon, M. J.; Shenoy, V. B.; Guduru, P. R. Quantifying capacity loss due to solid-electrolyte-interphase layer formation on silicon negative electrodes in lithium-ion batteries. *J. Power Sources* **2012**, *215*, 145–151.
- (13) Jin, Y.; et al. Self-healing SEI enables full-cell cycling of a silicon-majority anode with a coulombic efficiency exceeding 99.9%. *Energy Environ. Sci.* **2017**, *10*, 580–592.
- (14) Yao, Y.; Liu, N.; McDowell, M. T.; Pasta, M.; Cui, Y. Improving the cycling stability of silicon nanowire anodes with conducting polymer coatings. *Energy Environ. Sci.* **2012**, *5*, 7927–7930.
- (15) Wang, W.; Gu, L.; Qian, H.; Zhao, M.; Ding, X.; Peng, X.; Sha, J.; Wang, Y. Carbon-coated silicon nanotube arrays on carbon cloth as a hybrid anode for lithium-ion batteries. *J. Power Sources* **2016**, *307*, 410–415.
- (16) Xu, Q.; Li, J.-Y.; Sun, J.-K.; Yin, Y.-X.; Wan, L.-J.; Guo, Y.-G. Watermelon-Inspired Si/C Microspheres with Hierarchical Buffer Structures for Densely Compacted Lithium-Ion Battery Anodes. *Adv. Energy Mater.* **2017**, *7*, 1601481.
- (17) Rong, Jiepeng; Fang, Xin; Mingyuan, Xu; Jing, Chen Coaxial Si/anodic titanium oxide/Si nanotube arrays for lithium-ion/battery anodes. *Nano Res.* **2013**, *6*, 182–190.
- (18) Tong, Y.; Xu, Z.; Liu, C.; Zhang, G. A.; Wang, J.; Wu, Z. G. Magnetic sputtered amorphous Si/C multilayer thin films as anode materials for lithium ion batteries. *J. Power Sources* **2014**, *247*, 78–83.
- (19) Li, J.; Dudney, N. J.; Nanda, J.; Liang, C. Artificial solid electrolyte interphase to address the electrochemical degradation of silicon electrodes. *ACS Appl. Mater. Interfaces* **2014**, *6*, 10083–10088.
- (20) Wu, H.; Yu, G.; Pan, L.; Liu, N.; McDowell, M. T.; Bao, Z.; Cui, Y. Stable Li-ion battery anodes by in-situ polymerization of conducting hydrogel to conformally coat silicon nanoparticles. *Nat. Commun.* **2013**, *4*, 1943.
- (21) Lu, Z.; et al. Nonfilling carbon coating of porous silicon micrometer-sized particles for high-performance lithium battery anodes. *ACS Nano* **2015**, *9*, 2540–2547.
- (22) Yi, R.; Chen, S.; Song, J.; Gordin, M. L.; Manivannan, A.; Wang, D. High-Performance Hybrid Supercapacitor Enabled by a High-Rate Si-based Anode. *Adv. Funct. Mater.* **2014**, *24*, 7433–7439.
- (23) Choi, J. W.; Aurbach, D. Promise and reality of post-lithium-ion batteries with high energy densities. *Nat. Rev. Mater.* **2016**, *1*, 16013.
- (24) Sun, W.; et al. Two-Dimensional Tin Disulfide Nanosheets for Enhanced Sodium Storage. *ACS Nano* **2015**, *9*, 11371–11381.
- (25) Yang, C. P.; Xin, S.; Yin, Y. X.; Ye, H.; Zhang, J.; Guo, Y. G. An advanced selenium-carbon cathode for rechargeable lithium-selenium batteries. *Angew. Chem.* **2013**, *125*, 8521–8525.
- (26) Eom, K.; Lee, J. T.; Oschatz, M.; Wu, F.; Kaskel, S.; Yushin, G.; Fuller, T. F. A stable lithiated silicon-chalcogen battery via synergetic chemical coupling between silicon and selenium. *Nat. Commun.* **2017**, *8*, 13888.
- (27) Qu, Y.; Zhang, Z.; Jiang, S.; Wang, X.; Lai, Y.; Liu, Y.; Li, J. Confining selenium in nitrogen-containing hierarchical porous carbon for high-rate rechargeable lithium-selenium batteries. *J. Mater. Chem. A* **2014**, *2*, 12255–12261.
- (28) Liu, T.; Dai, C.; Min, J.; Liu, D.; Bao, S.-J.; Jian, J.; Xu, M.; Li, C. Selenium Embedded in MOFs-derived Hollow Hierarchical Porous Carbon Spheres for Advanced Lithium-selenium Batteries. *ACS Appl. Mater. Interfaces* **2016**, *8*, 16063.
- (29) Zheng, G.; Xiang, Y.; Xu, L.; Luo, H.; Wang, B.; Liu, Y.; Han, X.; Zhao, W.; Chen, S.; Chen, H.; Zhang, Q.; Zhu, T.; Yang, Y. Controlling Surface Oxides in Si/C Nanocomposite Anodes for High-Performance Li-Ion Batteries. *Adv. Energy Mater.* **2018**, *8*, 1801718.
- (30) Liu, J.; Qiao, S. Z.; Liu, H.; Chen, J.; Orpe, A.; Zhao, D.; Lu, G. Q. Extension of the Stober method to the preparation of monodisperse resorcinol-formaldehyde resin polymer and carbon spheres. *Angew. Chem., Int. Ed.* **2011**, *50*, 5947–5951.
- (31) Guo, S.; Hu, X.; Hou, Y.; Wen, Z. Tunable Synthesis of Yolk-shell Porous-silicon@Carbon for Optimizing Si/C-based Anode of Lithium-Ion Batteries. *ACS Appl. Mater. Interfaces* **2017**, *9*, 42084–42092.
- (32) Yi, Z.; Yuan, L.; Sun, D.; Li, Z.; Wu, C.; Yang, W.; Wen, Y.; Shan, B.; Huang, Y. High-performance lithium-selenium batteries promoted by heteroatom-doped microporous carbon. *J. Mater. Chem. A* **2015**, *3*, 3059–3065.
- (33) Liu, T.; Zhang, Y.; Hou, J.; Lu, S.; Jiang, J.; Xu, M. High performance mesoporous C@Se composite cathodes derived from Ni-based MOFs for Li-Se batteries. *RSC Adv.* **2015**, *5*, 84038–84043.
- (34) Shen, D.; Huang, C.; Gan, L.; Liu, J.; Gong, Z.; Long, M. Rational Design of Si@SiO₂/C Composites Using Sustainable Cellulose as a Carbon Resource for Anodes in Lithium-Ion Batteries. *ACS Appl. Mater. Interfaces* **2018**, *10*, 7946–7954.
- (35) Liang, J.; Li, X.; Hou, Z.; Zhang, W.; Zhu, Y.; Qian, Y. A Deep Reduction and Partial Oxidation Strategy for Fabrication of Mesoporous Si Anode for Lithium Ion Batteries. *ACS Nano* **2016**, *10*, 2295–2304.
- (36) Zeng, L.; Wei, X.; Wang, J.; Jiang, Y.; Li, W.; Yu, Y. Flexible one-dimensional carbon-selenium composite nanofibers with superior electrochemical performance for Li-Se/Na-Se batteries. *J. Power Sources* **2015**, *281*, 461–469.
- (37) Li, Z.; Yuan, L.; Yi, Z.; Liu, Y.; Huang, Y. Confined selenium within porous carbon nanospheres as cathode for advanced Li-Se batteries. *Nano Energy* **2014**, *9*, 229–236.
- (38) Gao, H.; Zhou, T.; Zheng, Y.; Zhang, Q.; Liu, Y.; Chen, J.; Liu, H.; Guo, Z. CoS Quantum Dot Nanoclusters for High-Energy Potassium-Ion Batteries. *Adv. Funct. Mater.* **2017**, *27*, 1702634.

- (39) Wang, J.; Zhou, M.; Tan, G.; Chen, S.; Wu, F.; Lu, J.; Amine, K. Encapsulating micro-nano Si/SiO_x into conjugated nitrogen-doped carbon as binder-free monolithic anodes for advanced lithium ion batteries. *Nanoscale* **2015**, *7*, 8023–8034.
- (40) Wang, D.; Gao, M.; Pan, H.; Wang, J.; Liu, Y. High performance amorphous-Si@SiO_x/C composite anode materials for Li-ion batteries derived from ball-milling and in situ carbonization. *J. Power Sources* **2014**, *256*, 190–199.
- (41) Li, M.; Gu, J.; Feng, X.; He, H.; Zeng, C. Amorphous-silicon@silicon oxide/chromium/carbon as an anode for lithium-ion batteries with excellent cyclic stability. *Electrochim. Acta* **2015**, *164*, 163–170.
- (42) Park, M. S.; Park, E.; Lee, J.; Jeong, G.; Kim, K. J.; Kim, J. H.; Kim, Y. J.; Kim, H. Hydrogen silsequioxane-derived Si/SiO_x nanospheres for high-capacity lithium storage materials. *ACS Appl. Mater. Interfaces* **2014**, *6*, 9608–9613.
- (43) Wang, J.; Bao, W.; Ma, L.; Tan, G.; Su, Y.; Chen, S.; Wu, F.; Lu, J.; Amine, K. Scalable Preparation of Ternary Hierarchical Silicon Oxide-Nickel-Graphite Composites for Lithium-Ion Batteries. *ChemSusChem* **2015**, *8*, 4073–4080.
- (44) Ren, Y.; Li, M. Si-SiO_x-Cristobalite/Graphite Composite as Anode for Li-ion Batteries. *Electrochim. Acta* **2014**, *142*, 11–17.
- (45) Su, J.; Zhao, J.; Li, L.; Zhang, C.; Chen, C.; Huang, T.; Yu, A. Three-Dimensional Porous Si and SiO₂ with In Situ Decorated Carbon Nanotubes As Anode Materials for Li-ion Batteries. *ACS Appl. Mater. Interfaces* **2017**, *9*, 17807–17813.
- (46) Liu, Z.; Yu, Q.; Zhao, Y.; He, R.; Xu, M.; Feng, S.; Li, S.; Zhou, L.; Mai, L. Silicon oxides: a promising family of anode materials for lithium-ion batteries. *Chem. Soc. Rev.* **2019**, *48*, 285–309.
- (47) Guo, J. J.; Morris, J. R.; Ihm, Y.; Contescu, C. I.; Gallego, N. C.; Duscher, G.; Pennycook, S. J.; Chisholm, M. F. Topological Defects: Origin of Nanopores and Enhanced Adsorption Performance in Nanoporous Carbon. *Small* **2012**, *8*, 3283–3288.
- (48) Zeng, Z. Y.; Liang, W. I.; Liao, H. G.; Xin, H. L. L.; Chu, Y. H.; Zheng, H. M. Visualization of Electrode-Electrolyte Interfaces in LiPF₆/EC/DEC Electrolyte for Lithium Ion Batteries via in Situ TEM. *Nano Lett.* **2014**, *14*, 1745–1750.
- (49) Kishida, I.; et al. First-principles calculations of migration energy of lithium ions in halides and chalcogenides. *J. Phys. Chem. B* **2006**, *110*, 8258.